Materials Advances

ROYAL SOCIETY OF CHEMISTRY

PAPER

View Article Online
View Journal

Check for updates

Cite this: DOI: 10.1039/d6ma00092d

Open Access Article. Published on 29 June 2026. Downloaded on 6/30/2026 1:33:55 AM. This article is licensed under a Creative Commons Attribution 3.0 Unported Licence.

AACVD-fabricated Zn-modified WO_3 photoanodes for enhanced solar water oxidation

Salma F. Alqahtani, †*[ab] Hussam M. Alzahrani[c] and Abdullah M. Alotaibi †*[c]

Received 21st January 2026,
Accepted 19th May 2026

DOI: 10.1039/d6ma00092d

rsc.li/materials-advances

The photoelectrochemical (PEC) performance of WO_3 photoanodes is limited by poor charge transport and high recombination losses. In this work, Zn-modified WO_3 thin films (0, 2, 10, and 20 wt%) were fabricated *via* a two-step aerosol-assisted chemical vapour deposition (AACVD) method to investigate the effect of Zn incorporation on material properties and PEC water oxidation performance. The 10 wt% Zn–WO_3 film exhibited the highest photocurrent density (0.68 mA cm^{-2} at 1.23 V_{RHE} under 1-sun illumination), corresponding to an enhancement of over 70% compared to pristine WO_3. This improvement is associated with nanorod morphology, enhanced (002) preferred orientation, bandgap narrowing (2.50 eV), and increased donor density, which promote more efficient charge transport and interfacial charge transfer. Electrochemical impedance and Mott–Schottky analyses further confirm reduced interfacial resistance and increased carrier density for the optimised composition. These results demonstrate that Zn doping improves the PEC water oxidation performance of WO_3 photoanodes.

1. Introduction

From a sustainability and environmental perspective, hydrogen is promoted as a sustainable and green alternative to fossil fuel-dependent energy systems. However, the current mature production routes are not yet entirely green.[1–3] Photoelectrochemical (PEC) water splitting has gained significant attention as a promising strategy for direct solar-to-hydrogen conversion since the pioneering work of Fujishima and Honda in 1972.[4] Despite this potential, the overall efficiency of PEC devices is primarily limited by the oxygen evolution reaction (OER) at the photoanode, which is kinetically sluggish and involves complex multi-electron transfer processes.[5–7]

Metal oxide semiconductors have been extensively explored as photoanode candidates due to their abundance, stability under oxidative conditions, and tunable electronic properties.[8–11] However, their performance is often constrained by poor charge–carrier mobility, rapid electron–hole recombination, and limited visible light absorption.[11–14] These limitations hinder efficient charge separation and transfer, which are essential for driving water oxidation. To address these challenges, various material engineering strategies have been developed, including co-catalyst loading, heterostructure design, and elemental doping.[15–23] Among these, doping is an effective approach to tailor the electronic structure and defect chemistry of semiconductors, enabling improved carrier concentration, reduced recombination, and enhanced charge transport.[24–26] In addition, doping can influence surface morphology and increase the density of active sites, further facilitating interfacial charge transfer during the OER.[27]

Tungsten trioxide (WO_3) is a promising n-type semiconductor for PEC water oxidation due to its suitable valence band position, visible light absorption up to *ca.* 477 nm (bandgap: ∼2.5–2.8 eV), and relatively high chemical stability compared to other photoanodes such as TiO_2 and $BiVO_4$.[28–32] However, its practical performance is limited by high recombination rates, inefficient charge transport, and an unfavourable conduction band position for hydrogen evolution.[33–35] These limitations prevent WO_3 from achieving its theoretical photocurrent, necessitating further optimisation through material modification.[34–40] Among various dopants, zinc (Zn) has attracted attention due to its ability to modify both the electronic structure and defect landscape of WO_3. The incorporation of Zn^{2+} can induce charge imbalance and promote the formation of oxygen vacancies, which enhance electrical conductivity and charge transport.[41] In addition, Zn-related donor states can increase carrier density and improve charge separation, leading to enhanced photocurrent response compared to pristine WO_3.[42,43]

The synthesis method plays a critical role in determining the structural and functional properties of WO_3 thin films. Conventional techniques, such as hydrothermal, sol–gel, sputtering, and pulsed laser deposition, often involve complex procedures or limited scalability.[44–49] In contrast, aerosol-

---

[a] Center of Excellence for Advanced Materials and Manufacturing, King Abdulaziz City for Science and Technology (KACST), Riyadh, 11442, Saudi Arabia. E-mail: sfalqahtani@kacst.gov.sa

[b] Advanced Materials Technologies Institute, King Abdulaziz City for Science and Technology (KACST), Riyadh, 11442, Saudi Arabia

[c] Hydrogen Technologies Institute, King Abdulaziz City for Science and Technology (KACST), Riyadh, 11442, Saudi Arabia. E-mail: abalotaibi@kacst.gov.sa

† These authors contributed equally.

© 2026 The Author(s). Published by the Royal Society of Chemistry

Open Access Article. Published on 29 June 2026. Downloaded on 6/30/2026 1:33:55 AM. This article is licensed under a Creative Commons Attribution 3.0 Unported Licence.

assisted chemical vapour deposition (AACVD) offers a versatile and scalable approach for producing thin films with controlled composition and morphology.[50] In this process, precursor solutions are atomised into aerosol droplets and transported to a heated substrate, where they decompose to form uniform films with tunable properties.[51]

Zn-modified WO_3 thin films with varying Zn contents (0, 2, 10, and 20 wt%) were synthesised using AACVD to examine how Zn incorporation influences the structural and photoelectrochemical properties of WO_3 photoanodes. Zn doping was found to alter the electronic structure and enhance charge transport, resulting in improved photoelectrochemical water oxidation performance. Among the samples, the 10 wt% Zn–WO_3 film showed the highest photocurrent density. These findings highlight the role of Zn in tuning the structural and PEC characteristics of WO_3. To the best of our knowledge, this is the first report of Zn-modified WO_3 films prepared by AACVD for solar-driven water oxidation.

2. Experimental

2.1. Materials

All chemicals and reagents utilised in this study were sourced from Sigma-Aldrich and used as received without further purification. Fluorine-modified tin oxide (FTO) glasses were used as conductive substrates for the preparation of the photoanodes. Before the films were deposited, the substrates were subjected to thorough ultrasonic cleaning to ensure their cleanliness. This procedure involved successive 10-minute rinses with acetone and isopropanol to remove organic residues. This was followed by a final rinse with deionised water to eliminate any remaining traces of solvents. The substrates were then dried under ambient conditions to prepare them for the subsequent steps of material deposition and characterisation.

2.2. Preparation of photoanodes

Employing aerosol-assisted chemical vapour deposition (AACVD), unmodified and Zn-modified WO_3 photoanodes were prepared. The detailed description of the AACVD experimental setup has been documented in the literature.[52,53] As depicted in Fig. 1a, AACVD proficiently combines aerosol generation with chemical deposition. In general, AACVD uses an ultrasonic atomiser to convert a liquid precursor solution into a fine aerosol mist. This aerosol is then transported into a reaction chamber through a gas carrier, which directs the aerosol droplets across a heated substrate. Upon contact, the droplets evaporate rapidly, decomposing the precursor and forming a uniform thin film.[53]

Initially, unmodified WO_3 films were deposited on FTO substrates by dissolving 0.2 g of tungsten hexacarbonyl [$W(CO)_6$] in a 45 mL mixture of acetone and methanol (2 : 1 ratio) in a glass bubbler. This solution was then placed on an ultrasonic humidifier equipped with a piezoelectric device (Johnson Matthey Liquifog) to generate the aerosol. A nitrogen gas (N_2, BOC Ltd.) flow of 1 L min^{-1} was used to transport the aerosol to the chamber, where the FTO substrates were heated at 350 °C. Following about 45 minutes of deposition, during which all the precursors were transferred, the substrates were cooled under a N_2 flow to below 100 °C. The substrates were subsequently heat-treated at 530 °C to enhance the crystallisation and oxidation of WO_3.

For the fabrication of Zn-modified WO_3 films, a second deposition procedure was applied on the pre-deposited WO_3 layer. A similar quantity of $W(CO)_6$ was dissolved in 30 mL of acetone and mixed with zinc chloride ($ZnCl_2$) in different molar ratios (2, 10, and 20 wt%) in 15 mL of methanol in three separate experiments to prepare the doping solutions. These solutions, with Zn dopant concentrations of 2%, 10% and 20%, were deposited at 420 °C to incorporate Zn into the WO_3 lattice. The films were then cooled and annealed following the same conditions as those used for pristine WO_3.

2.3. Physical characterisation

The crystalline structure and phase composition of the pristine and Zn-modified WO_3 films were analysed by X-ray diffraction (XRD) using a modified Bruker AXS D8 diffractometer with Cu Kα radiation (λ = 1.5406 Å), operated at 40 kV and 30 mA. The scans were performed in the 2θ range of 10°–80° in increments of 0.02°. Field emission scanning electron microscopy (FESEM, JEOL JSM-6301F, 5 kV) was employed to observe the surface morphology; the samples were coated with a thin Au layer to reduce charging. Energy dispersive X-ray spectroscopy (EDX) was carried out using the same JEOL JSM-6301F FESEM equipped with an EDX detector to confirm the elemental composition. Surface topography and roughness were assessed using atomic force microscopy (AFM, Bruker Dimension Icon) in tapping mode. Optical absorption spectra were recorded in the 200–800 nm range using an Agilent Cary 60 UV-vis spectrophotometer. Photoluminescence (PL) spectra were measured at room temperature using a HORIBA TCSPC fluorometer at an excitation wavelength of 325 nm, with emission recorded from 380 to 800 nm.

2.4. Photoelectrochemical characterisation

The PEC performance of pristine and Zn-modified WO_3 photoanodes was evaluated in a conventional three-electrode configuration using a Metrohm Autolab potentiostat. The working electrode comprised the WO_3-coated substrate, with a platinum wire and an Ag/AgCl (3 M KCl) electrode serving as the counter and reference electrodes, respectively. All measurements were conducted in 1.0 M KOH aqueous electrolyte (pH ≈ 14) at room temperature. The geometric area exposed to illumination was restricted to 1 cm^2. Linear sweep voltammetry (LSV) was performed under simulated AM 1.5G solar illumination (100 mW cm^{-2}) using a xenon lamp. The scans were recorded at a rate of 10 mV s^{-1} within the potential window of 0.2 to 1.6 V_{RHE}. The dark response was also acquired under identical conditions. Potentials measured against the Ag/AgCl electrode were converted to the reversible hydrogen electrode (RHE) scale using the Nernst equation:

$$E_{\mathrm{RHE}} = E_{\mathrm{Ag/AgCl}} + (0.059 \times \mathrm{pH}) + E^{\circ}_{\mathrm{Ag/AgCl}} \quad (1)$$

© 2026 The Author(s). Published by the Royal Society of Chemistry

Open Access Article. Published on 29 June 2026. Downloaded on 6/30/2026 1:33:55 AM. This article is licensed under a Creative Commons Attribution 3.0 Unported Licence.

where $E_{\mathrm{Ag/AgCl}}$ is the potential measured against the Ag/AgCl electrode and $E^{\circ}_{\mathrm{Ag/AgCl}} = 0.197$ V under standard conditions.

Mott–Schottky (M–S) measurements were conducted under visible light illumination at a fixed frequency of 1 kHz with a 10 mV AC perturbation. An apparent flat-band potential (E_{fb}) and donor density (N_{D}) were determined from the linear region of the $1/C^2$ *versus* potential plot using the standard Mott–Schottky relation. Electrochemical impedance spectroscopy (EIS) was carried out under illumination at a fixed bias of 1.23 $\mathrm{V_{RHE}}$ over the frequency range of 0.1 Hz to 100 kHz.

3. Results and discussion

This work explored aerosol-assisted chemical vapour deposition (AACVD) as a synthesis-driven strategy for engineering WO_3 thin films with tunable composition and functionality. Introducing Zn during film growth modified the physicochemical properties of WO_3 at the deposition stage, providing a direct route to engineer the photoanode material. The resulting films were then evaluated for photoelectrochemical (PEC) water oxidation to assess their potential as high-performance photoanodes.

Pristine WO_3 and Zn–WO_3 films were successfully synthesised using our home-built AACVD system under optimised conditions (Fig. 1a). A two-step deposition approach was used: an initial base layer of pristine WO_3 was deposited at 350 °C, followed by a Zn-incorporated WO_3 top layer deposited at 420 °C using precursor solutions containing 2, 10 and 20 wt% Zn. The resulting dark blue films were then annealed at 530 °C in air to improve crystallinity. The annealed samples exhibited a uniform pale-yellow colour, which became more intense with increasing Zn content. The increased intensity may suggest a change in the band structure or oxygen vacancy density. This controlled deposition produced smooth, well-adhered films with no visible cracks or delamination.

The crystalline phases of the deposited films were identified by XRD analysis. As shown in Fig. 1b, all films exhibit diffraction peaks that match well with monoclinic WO_3 (ICSD file no. 1620). For pristine WO_3, the main peaks appear at $2\theta \approx 23.9^{\circ}$, 24.5° and 25.2°, corresponding to the (002), (020) and (200) planes, respectively, confirming the formation of monoclinic WO_3.[54,55] Slight deviations from the reference peak positions may be related to minor lattice distortion associated with the deposition process.[56] In addition, the relatively high intensity of the (020) peak in the unmodified film suggests preferred orientation along this plane.[57–59] The monoclinic structure was retained after Zn addition. A slight shift toward higher 2θ was observed only for the 2% Zn–WO_3 film. According to Bragg's law, this indicates a small decrease in *d*-spacing, which can be attributed to local lattice strain or defect formation caused by low-level Zn incorporation during film growth. This shift was not clearly observed in the 10% and 20% Zn–WO_3 films. Importantly, all Zn-containing films still showed the characteristic diffraction peaks of monoclinic WO_3, with no new dominant peaks indicating a change in the main crystal phase. A change in relative peak intensity was also observed after Zn addition, with the (002) reflection becoming more prominent relative to (020). Overall, the XRD results indicate that Zn addition affected the peak position and relative intensity only slightly.

The surface properties were then investigated using SEM and AFM analyses. As presented in Fig. 1(d–g), the SEM images demonstrate that Zn doping modifies the surface morphology of WO_3 films deposited by AACVD. The unmodified WO_3 film (Fig. 1d) displays densely packed, vertical-aligned nanorods with slightly tapered tips. This structure facilitates efficient directional charge transport but may still offer limited active surface area. With the introduction of Zn, the growth of WO_3 nanorods exhibited a noticeable change in morphology. At 10% Zn (Fig. 1f), the film exhibits sharper, spike-like nanorods with increased surface roughness and more exposed active edges. Such features help enhance charge separation and accelerate OER kinetics. However, excess Zn content (20% Zn, Fig. 1g) results in aggregated, cluster-like ends, which in turn impede charge transfer and increase charge recombination losses. These findings confirm that moderate doping optimises the surface morphology, which helps enhance water oxidation activity. In addition, the EDX spectrum of 10% Zn-modified WO_3 presented in Fig. 1c verifies the presence of W, O and Zn elements, confirming that Zn is well incorporated into the WO_3 lattice.

The surface topography, roughness, and surface area of the prepared films were examined using AFM measurements. The two-dimensional AFM images in Fig. 2 highlight noticeable changes in surface texture following Zn doping. As observed in Fig. 2a, the unmodified WO_3 film exhibits relatively regular grains and a smooth, compact surface with minor height variations. In contrast, as Zn concentration increases (Fig. 2b–d), the grain structure becomes less regular, the grain size increases, the surface roughness increases, and the topographical features become more significant with greater height variations. The roughness parameters and surface area values extracted from AFM analysis are summarised in Table 1, reflecting clearly the influence of Zn content on the film's surface texture.

The optical absorption behaviour of pristine and Zn-modified WO_3 films was evaluated using UV-vis spectroscopy, as shown in Fig. 3a. All samples exhibit strong absorption in the UV region, with a clear red shift in the absorption edge upon Zn incorporation. The optical bandgap was estimated by plotting $(\alpha h\nu)^{1/n}$ against $h\nu$ using $n = 2$ for an indirect bandgap transition.[39] The extrapolated bandgaps decreased from 2.76 eV for pristine WO_3 to 2.68, 2.50 and 2.58 eV for the 2%, 10% and 20% Zn-modified films, respectively, as shown in the inset of Fig. 3a. The narrowing of the bandgap with Zn incorporation, particularly at 10% doping, suggests the introduction of defect intermediate states and band tailing effects that lower the energy required for electronic excitation. These modifications enhance absorption in the visible region and may contribute to improved photo-response under solar irradiation.

To gain insight into the charge carrier dynamics and recombination behaviour, PL measurements were carried out at room temperature. Fig. 3b displays the PL spectra of unmodified WO_3 and Zn-modified WO_3 films with various Zn concentrations,

Open Access Article. Published on 29 June 2026. Downloaded on 6/30/2026 1:33:55 AM.
This article is licensed under a Creative Commons Attribution 3.0 Unported Licence.

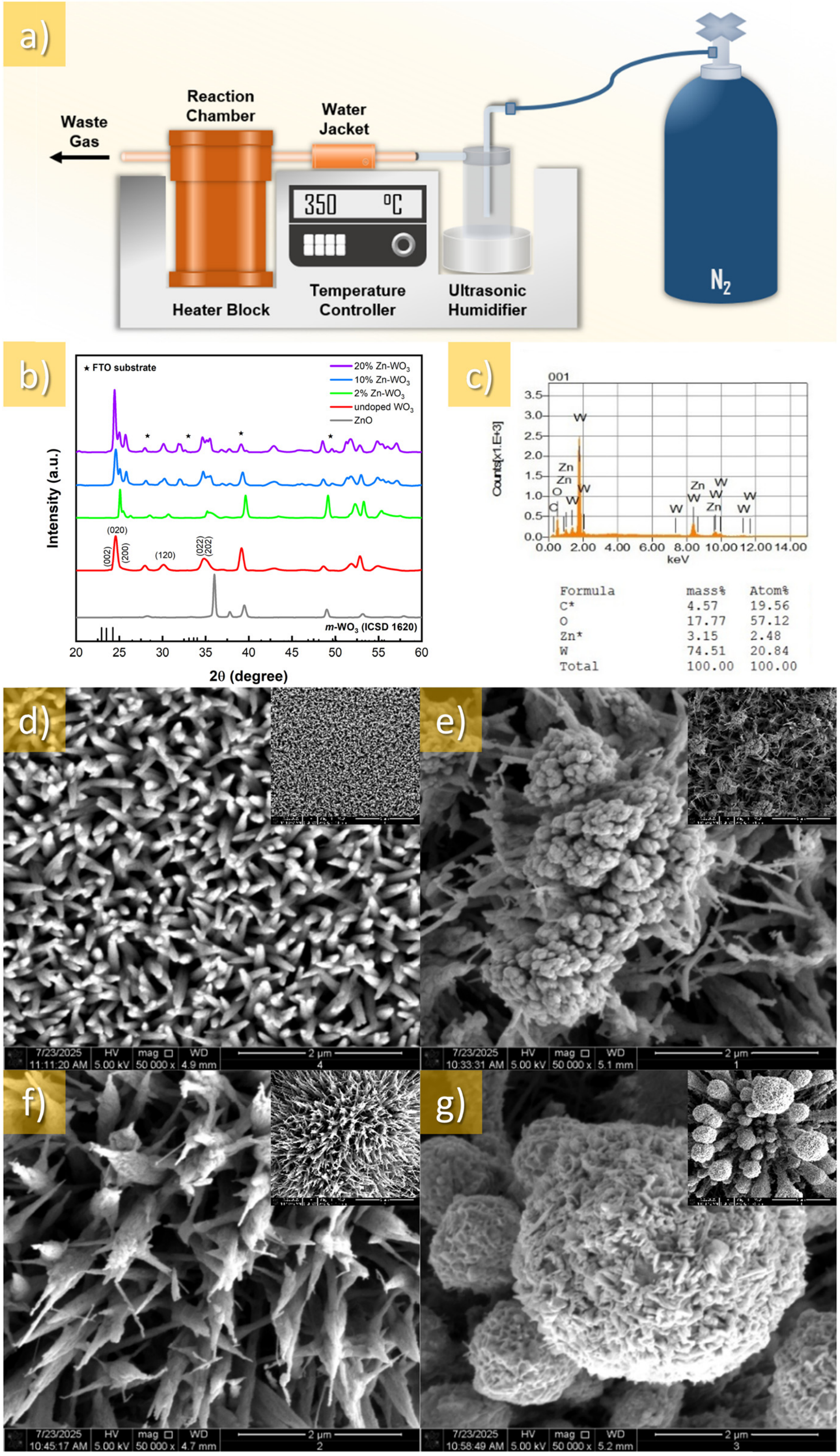

Formula	mass%	Atom%
C*	4.57	19.56
O	17.77	57.12
Zn*	3.15	2.48
W	74.51	20.84
Total	100.00	100.00

Fig. 1 Schematic illustration of the AACVD reactor setup used for the deposition of WO_3 and Zn-modified WO_3 thin films (a). XRD patterns of WO_3 and Zn-modified WO_3 (2%, 10% and 20%) (b). EDX spectrum of 10% Zn-modified WO_3 with data given below (c). Surface SEM images of pure WO_3 (d) and 2% (e), 10% (f), and 20% (g) Zn-modified WO_3 films.

recorded under 325 nm excitation. The unmodified film shows a strong emission centred at ∼435 nm, which is usually associated with radiative recombination through intrinsic defects, mainly oxygen vacancies.[60,61] In contrast, the Zn-modified WO_3 samples exhibit a clear decrease in PL intensity and a slight red shift of the emission peak towards ∼455 nm.

© 2026 The Author(s). Published by the Royal Society of Chemistry

Open Access Article. Published on 29 June 2026. Downloaded on 6/30/2026 1:33:55 AM.
This article is licensed under a Creative Commons Attribution 3.0 Unported Licence.

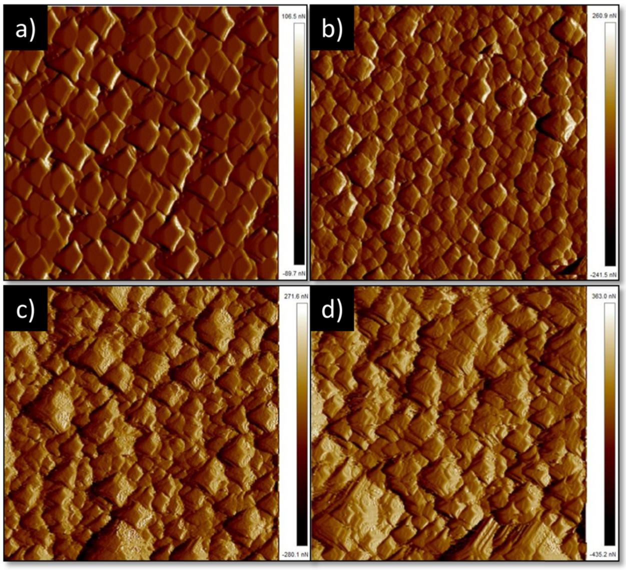

Fig. 2 Two-dimensional AFM surface topography images of pristine WO_3 (a) and 2% (b), 10% (c) and 20% (d) Zn-modified WO_3 films.

Table 1 AFM surface roughness parameters (R_{max}, R_q and R_a) and surface area of the pristine and Zn-modified WO_3 thin films (measuring range: 10 × 10 μm^2)

Samples	Surface roughness (nm)			Surface area (μm^2)
	R_{max}	R_q	R_a	
20% Zn–WO_3	2783	359	282	167
10% Zn–WO_3	2407	301	225	166
2% Zn–WO_3	1245	99	73	119
Pristine WO_3	355	53.3	42.5	29

This reduction in intensity reflects a lower recombination rate of photogenerated electron–hole pairs, implying improved charge separation in the modified films.[62] The observed PL quenching becomes most pronounced at 10% and 20% Zn doping, suggesting the formation of additional defect or trap states that act as non-radiative recombination centres. These are likely introduced by the aliovalent substitution of W^{6+} with Zn^{2+}, which causes local structural distortion and induces oxygen vacancies for charge compensation. The redshift and broadening of the emission further support an increase in structural disorder, consistent with observations from XRD and UV-vis analysis.

XPS analysis confirms the successful incorporation of Zn into WO_3 while largely preserving the WO_3 chemical framework. In the W 4f region (Fig. 4a) for the 10% Zn–WO_3 sample, the spectrum exhibits the characteristic spin–orbit doublet with peaks centred at 35.5 eV (W $4f_{7/2}$) and 37.6 eV (W $4f_{5/2}$), separated by 2.1 eV, which is typical of W^{6+} in stoichiometric WO_3. The absence of a pronounced low-binding-energy shoulder suggests that tungsten remains predominantly in the W^{6+} oxidation state, indicating that the host lattice is largely maintained after Zn addition. Any reduced W species such as W^{5+}/W^{4+}, if present, would be minor or unresolved at this scale. In the Zn 2p region (Fig. 4b–d for 10% Zn–WO_3, 20% Zn–WO_3 and 2% Zn–WO_3 samples, respectively), two well-defined peaks appear at 1022 eV and 1044.7 eV, corresponding to Zn $2p_{3/2}$ and Zn $2p_{1/2}$, respectively, with a spin–orbit splitting of 23 eV, consistent with Zn^{2+} in an oxide environment. Together, these results verify the presence of Zn in the modified sample and indicate that Zn is present in the Zn^{2+} state, while the tungsten environment remains predominantly W^{6+}–WO_3. Any Zn-induced charge compensation is therefore expected to occur mainly through subtle lattice distortion and/or the creation of oxygen vacancy-related defects, rather than extensive reduction of tungsten. The full survey spectrum of the 10% Zn–WO_3 thin film is presented in Fig. S1.

The PEC activity of unmodified and Zn-modified WO_3 thin films was examined under simulated 1-sun illumination (AM 1.5G) in a 1.0 M KOH electrolyte *via* LSV measurements. As illustrated in Fig. 5a, all films exhibited anodic photocurrents with negligible dark currents, confirming that the observed

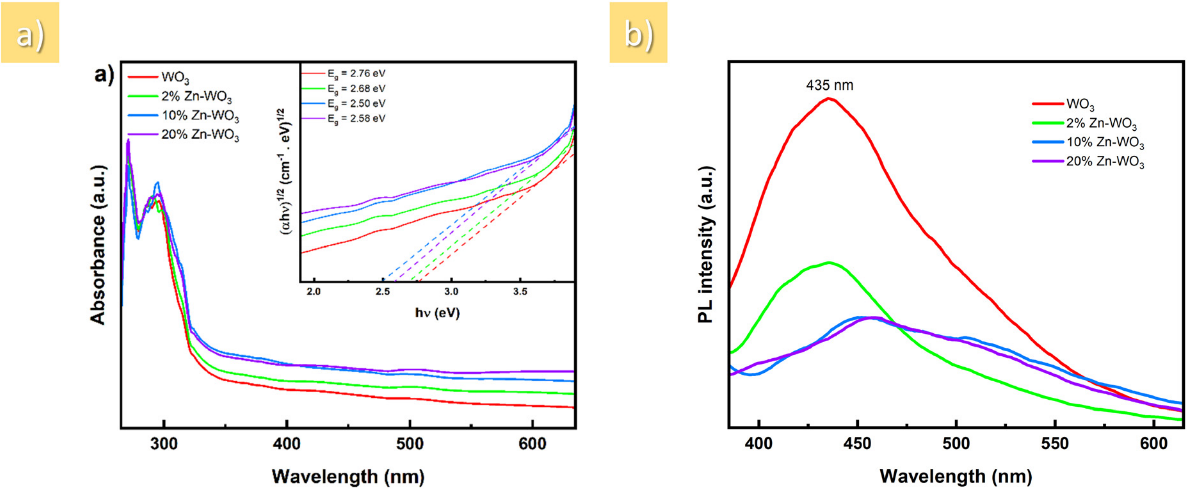

Fig. 3 UV-vis absorbance spectra with bandgap determination (a) and photoluminescence (PL) spectra (b) of unmodified and Zn-modified WO_3 films.

© 2026 The Author(s). Published by the Royal Society of Chemistry

Open Access Article. Published on 29 June 2026. Downloaded on 6/30/2026 1:33:55 AM.
This article is licensed under a Creative Commons Attribution 3.0 Unported Licence.

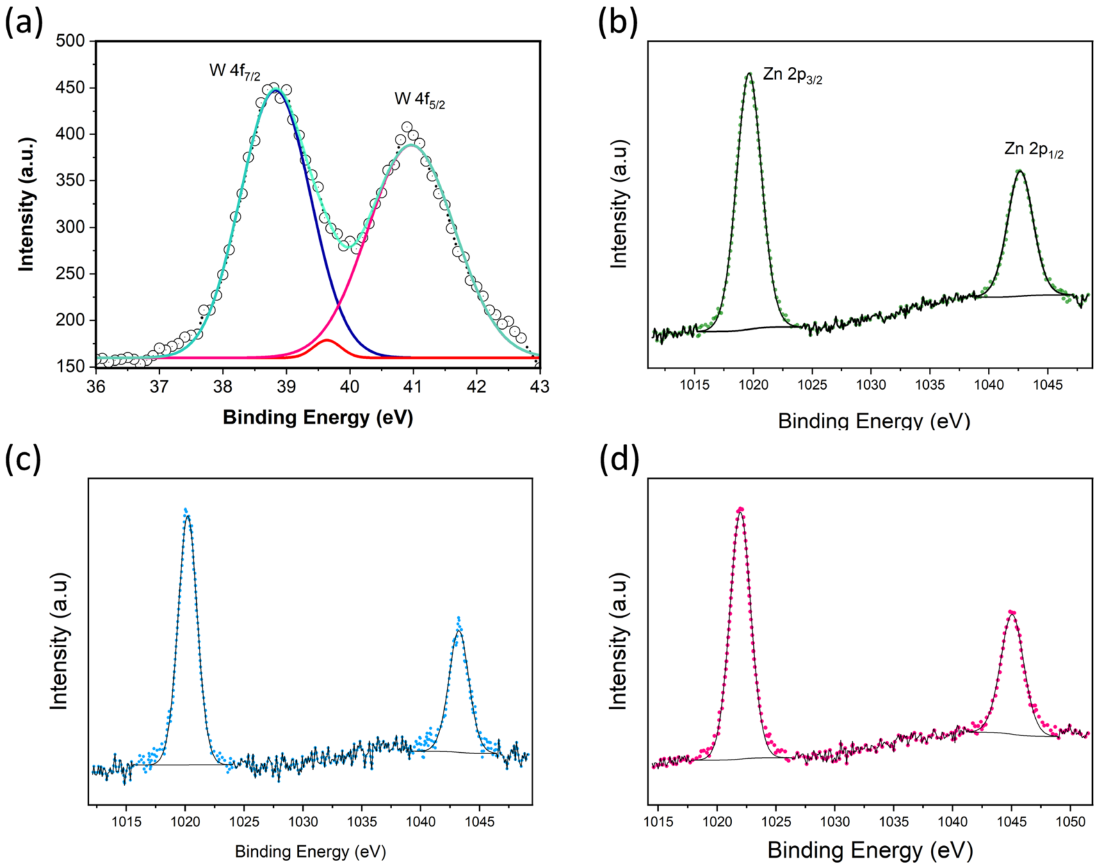

Fig. 4 Surface X-ray photoelectron spectroscopy (XPS) spectra of (a) W $4f_{7/2}$ and $4f_{5/2}$ for the 10% Zn–WO_3 sample and (b) Zn $2p_{3/2}$ and $2p_{1/2}$ core level scans in the 10% Zn modified WO_3 thin film, (c) Zn $2p_{3/2}$ and $2p_{1/2}$ core level scans in the 20% Zn modified WO_3 thin film and (d) Zn $2p_{3/2}$ and $2p_{1/2}$ core level scans in the 20% Zn modified WO_3 thin film.

responses originate exclusively from photoinduced charge–carrier interactions. The unmodified WO_3 film delivered a photocurrent density of $\sim$0.39 mA cm^{-2} at 1.23 V_{RHE}, with an onset potential around 0.70 V_{RHE}. This relatively reflects sluggish hole transfer at the interface and can be attributed to the compact morphology, low surface area and dominant (020) facet, which have been shown to limit the reaction kinetics and active site density.[63] The wide optical bandgap (2.76 eV) and strong PL emission also reflect limited visible-light absorption and high recombination losses, respectively.

In general, significant changes in PEC behaviours were observed in Zn-incorporated films. At low Zn concentration, the photocurrent dropped to $\sim$0.15 mA cm^{-2} at 1.23 V_{RHE}. This reduction does not follow the expected trend with Zn incorporation and may be associated with local structural distortion, as indicated by the slight shift in the XRD peaks. Such local lattice strain can introduce unfavourable electronic environments or trap sites that hinder effective charge transport and interfacial charge transfer. Despite the reduced bandgap (2.68 eV), these effects appear to limit the photocurrent response. Of all the films, the 10% Zn–WO_3 sample exhibited the highest photocurrent density at 1.23 V_{RHE} ($\sim$0.68 mA cm^{-2}) with an improved onset potential of $\sim$0.56 V_{RHE}. This improvement is attributed to enhanced visible-light absorption (E_g = 2.50 eV) and reduced electron–hole recombination as indicated by the quenched PL intensity. Furthermore, XRD analysis revealed a preferential shift in crystal orientation towards the (002) plane, which plays a crucial role in promoting OER kinetics. It is known that the (002) facet exposes a higher density of catalytically active terminal oxygen atoms and facilitates stronger orbital overlap with water molecules, thereby lowering the energy barrier for hole transfer and accelerating the formation of key reaction intermediates such as $OH^\bullet$ and $OOH^\bullet$.[64] In contrast, the (020) facet, which dominates in the unmodified film, is associated with fewer active sites and slower reaction kinetics at the surface.[65] This transition in crystal orientation coupled with the increased surface roughness and active area observed *via* AFM improves charge separation and interfacial charge transfer, ultimately leading to a more efficient and earlier PEC response. At a higher Zn content (20%), however, there is a renewed decrease in the photocurrent ($\sim$0.61 mA cm^{-2}), which is related to a lower surface roughness and a potential oversaturation of the dopant. Both can reduce the active (002) facet density or promote deep trap states. This suggests that facet exposure is critical but must be balanced by optimal doping to sustain structural integrity and carrier mobility.

This trend is demonstrated in Fig. 5b, which presents a bar chart comparing the photocurrent densities at 1.23 V_{RHE} for different Zn concentrations. The 10% Zn-modified WO_3 film

© 2026 The Author(s). Published by the Royal Society of Chemistry

Open Access Article. Published on 29 June 2026. Downloaded on 6/30/2026 1:33:55 AM.
This article is licensed under a Creative Commons Attribution 3.0 Unported Licence.

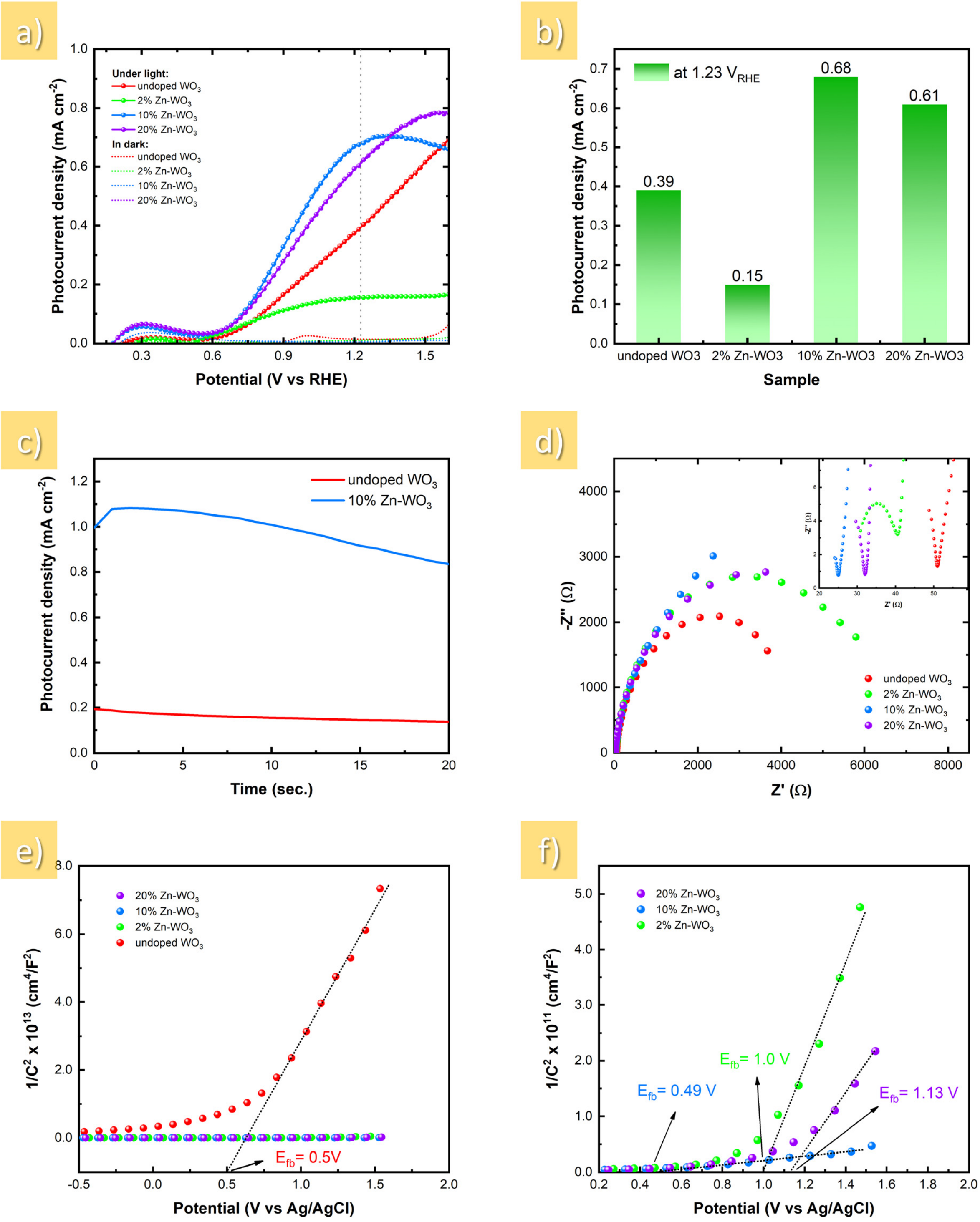

Fig. 5 Linear sweep voltammetry (LSV) curves under dark and illuminated conditions (a), the photocurrent density at 1.23 V_{RHE} for all samples (b), amperometric *I*–*t* curves at a potential of 1.08 V_{RHE} (c), Nyquist plots of electrochemical impedance spectra (d), and Mott–Schottky plots (e) and (f) under AM 1.5G illumination of the pristine WO_3 and Zn-modified WO_3 films.

shows the highest photocurrent density, confirming its superior photoelectrocatalytic activity. This improvement results from the optimisation of several key properties, including enhanced light absorption, improved crystal orientation, and refined surface morphology. These factors promote more efficient charge transfer and reduce the energy barrier for oxygen evolution. Table 2 further contextualises this performance by summarising reported photocurrent values for various modified WO_3 photoanodes and comparing them with the film developed in this study.

Under the same PEC experimental conditions, the stability of the 10% Zn-modified WO_3 film was evaluated and compared

Open Access Article. Published on 29 June 2026. Downloaded on 6/30/2026 1:33:55 AM.
This article is licensed under a Creative Commons Attribution 3.0 Unported Licence.

Table 2 Comparison of selected WO_3 photoanodes doped with various dopants and their PEC performance for water oxidation reported in the literature

Photoanode	Dopant, content	Synthesis technique	Morphology	Photocurrent performance	Electrolyte, illumination	Ref.
Zn-doped WO_3	Zn, 10 wt%	AACVD	Spike-like nanorods	0.68 mA cm^{-2} at 1.23 V_{RHE}	1 M KOH, AM 1.5G	This work
Ti-doped WO_3	Ti, 1.16 at%	Single-step hydrothermal	Nanoparticles	1.139 mA cm^{-2} at 1.23 V_{RHE}	0.1 M Na_2SO_4, AM 1.5G	66
In-doped WO_3	In, 3 wt%	Hydrothermal	Nanoblocks	2.18 mA cm^{-2} at 1.23 V_{RHE}	0.1 M Na_2SO_4, AM 1.5G	67
Ta-doped WO_3	Ta, 3.93 at%	Reactive magnetron co-sputtering	Granular with well-defined boundaries	0.65 mA cm^{-2} at 1.0 $V_{Ag/AgCl}$	0.2 M Na_2SO_4, AM 1.5G	68
Sn-doped WO_3	Sn, 0.80 at%	Single-step hydrothermal	Coagulated nanoparticles + plate-like structures	0.427 mA cm^{-2} at 1.23 V_{RHE}	0.5 M Na_2SO_4, AM 1.5G	69
Al-doped WO_3	Al, 0.77 at%	RF magnetron co-sputtering + hydrothermal	Nanoplates	1.14 mA cm^{-2} at 1.2 $V_{Ag/AgCl}$	0.5 M H_2SO_4, AM 1.5G	70
Ni-doped WO_3	Ni, 3 at%	Two-step hydrothermal	Nanoplate arrays	0.80 mA cm^{-2} at 1.0 $V_{Ag/AgCl}$	0.5 M Na_2SO_4, AM 1.5G	71
Cu-doped WO_3	Cu, 1.41 wt%	Hydrothermal	Nanoparticle assembly	0.487 mA cm^{-2} at 1.23 V_{RHE}	0.5 M Na_2SO_4, AM 1.5G	72
Co-doped WO_3	Co, 0.36 wt%	Hydrothermal	Nanorods and nanoparticles	0.636 mA cm^{-2} at 1.23 V_{RHE}	0.5 M Na_2SO_4, AM 1.5G	72
Gd-doped WO_3	Gd, 4%	Hydrothermal	Nanoplate arrays	2.28 mA cm^{-2} at 1.0 $V_{Ag/AgCl}$	0.2 M Na_2SO_4, AM 1.5G	73
Bi-doped WO_3	Bi, 0.17 at%	Modified hydrothermal	Porous nanoparticle film	1.51 mA cm^{-2} at 1.23 V_{RHE}	0.1 M Na_2SO_4, AM 1.5G	35

with that of pristine WO_3 at approximately 1.08 V_{RHE}, as shown in Fig. 5c. The Zn-modified film exhibited a higher and more stable photocurrent than the unmodified photoanode. This enhanced stability suggests more efficient charge transfer and suppressed surface recombination during PEC operation.

Post-PEC XRD patterns (Fig. S2) show reduced peak intensity, which may be due to partial dissolution of WO_3 in the highly alkaline electrolyte. The Zn-modified sample shows smaller changes compared to pristine WO_3, consistent with its higher and more stable photocurrent.

The EIS measurements were performed under illumination to assess the charge transfer characteristics at the interface of the photoanodes (Fig. 5d). All samples exhibited characteristic semicircular Nyquist arcs, representing the charge transfer resistance (R_{ct}) at the photoanode–electrolyte interface. Among all compositions, the 10% Zn–WO_3 sample displayed the smallest arc diameter, indicating the lowest R_{ct} and thus the most efficient interfacial charge transport. This reflects an enhancement in electrical conductivity and lower recombination losses, both of which contribute to the excellent PEC performance of this sample. In comparison, the pristine and 2% Zn–WO_3 films showed significantly larger arcs, suggesting slower charge transfer dynamics and lower conductivity. The high Zn content sample exhibited an intermediate arc size, suggesting that excessive doping impairs the interfacial transport, likely due to increased structural disorder or trap-state formation. The high-frequency region, magnified in the inset of Fig. 5d, provides valuable insight into the solution resistance (R_s). The 10% Zn-modified WO_3 film exhibited the lowest R_s among the films, showing enhanced electrolyte conductivity within the overall PEC system. This reduction in R_s further contributes to efficient charge extraction and minimised resistive losses.

To further probe the effects of doping on the electronic properties of Zn-modified WO_3 samples, Mott–Schottky analysis was conducted under illumination (Fig. 5e and f). The obtained plots exhibit linear regions with positive gradients for all samples, indicating that the materials behave as n-type semiconductors, where electrons are the dominant charge carriers. The flat band potential was determined by extrapolating the linear region to the potential axis. The estimated values were approximately 1.0 V for 2% Zn–WO_3, 0.49 V for 10% Zn–WO_3, and 1.13 V for 20% Zn–WO_3 (*vs.* Ag/AgCl). The observed shift in flat band potential with increasing Zn content suggests a modification in the electronic structure and a shift in the Fermi level position. Furthermore, the variation in the slope of the Mott–Schottky plots reflects differences in charge carrier density among the samples. In particular, the 10% Zn–WO_3 sample exhibits the lowest slope, suggesting an increase in effective carrier density or capacitance response compared to the other compositions. This enhancement in charge carrier density is expected to improve electrical conductivity and facilitate charge transport within the material.[74] From an electrochemical perspective, when a potential more positive than the flat band potential is applied to an n-type semiconductor, electron accumulation occurs at the electrode/electrolyte interface.[75] This promotes electron transfer towards the surface

Open Access Article. Published on 29 June 2026. Downloaded on 6/30/2026 1:33:55 AM.
This article is licensed under a Creative Commons Attribution 3.0 Unported Licence.

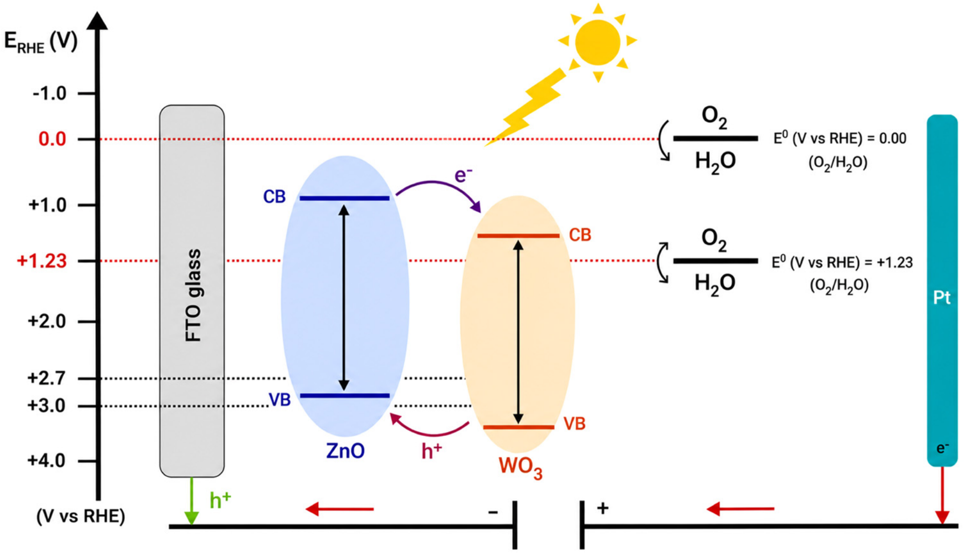

Fig. 6 Schematic representation of the mechanism of PEC water splitting in Zn modified WO_3 films on FTO substrates.

and enhances electrochemical reactions. Conversely, at potentials more negative than the flat band potential, charge depletion occurs, reducing the availability of electrons at the surface. This behaviour is governed by band bending at the semiconductor/electrolyte interface.[76,77] The lower flat band potential of the 10% Zn–WO_3 sample indicates that its Fermi level is closer to the conduction band, which results in a higher electron density. This increased electron density improves charge separation and facilitates electron transfer at the semiconductor/electrolyte interface.[78,79] Based on these results, the 10% Zn-modified WO_3 sample demonstrates superior electrochemical performance due to its favourable flat band potential and higher charge carrier density, which enhance interfacial charge transfer. These properties make it a promising candidate for applications such as photoelectrochemical systems and photocatalysis.

Fig. 6 illustrates the proposed mechanism for PEC water splitting using a Zn modified WO_3 thin film under light illumination. WO_3 is an n-type semiconductor with a relatively narrow bandgap (2.6–2.8 eV), and its valence band edge lies at a highly positive potential ($>$+3.0 V *vs.* RHE), well above the water oxidation potential (+1.23 V *vs.* RHE). This makes WO_3 highly suitable for driving the oxygen evolution reaction (OER). However, WO_3 alone is not capable of overall water splitting because its conduction band position is more positive than the H^+/H_2 reduction potential, limiting its ability to generate hydrogen. On the other hand, ZnO is an n-type semiconductor with a wider bandgap (3.2 eV) and a more negative conduction band edge, which is thermodynamically favorable for hydrogen evolution. Under illumination, electrons are excited from the valence band to the conduction band in both semiconductors, leaving behind holes in their respective valence bands. In the Zn modified WO_3 films, the band alignment promotes charge separation. The photogenerated electrons in the conduction band of ZnO can be efficiently transferred to the external circuit (*via* FTO and Pt), where they participate in the reduction of water to produce hydrogen. Meanwhile, the holes accumulated in the valence band of WO_3, due to its more positive potential, drive the oxidation of water to generate oxygen. This doping facilitates effective spatial separation of charge carriers, reduces electron–hole recombination, and enhances overall charge transfer efficiency.

4. Conclusion

To conclude, Zn-modified WO_3 thin films were successfully synthesised *via* a two-step AACVD method, and the effect of Zn incorporation on their structural, optical, and photoelectrochemical properties was investigated. Zn doping modifies the morphology, crystal orientation, and electronic properties of WO_3, leading to improved PEC performance for water oxidation. The 10 wt% Zn–WO_3 film exhibited the highest photocurrent density ($\sim$0.68 mA cm^{-2} at 1.23 V_{RHE}), together with improved onset potential and reduced interfacial resistance, which are attributed to bandgap narrowing, increased donor density, and enhanced charge transport. Overall, Zn incorporation enhances the PEC behaviour of WO_3 photoanodes under the tested conditions.

Author contributions

A. A. supervised the research, guided the experimental design, reviewed the manuscript, and provided scientific direction throughout the study. S. A. conducted the synthesis of the materials, performed all experiments, data analysis, and discussions, and wrote the manuscript. H. A. contributed to the synthesis of the samples.

Conflicts of interest

The authors declare that they have no conflicts of interest related to this work.

Open Access Article. Published on 29 June 2026. Downloaded on 6/30/2026 1:33:55 AM. This article is licensed under a Creative Commons Attribution 3.0 Unported Licence.

Data availability

The data that support the findings of this study are available within the article and its supplementary information (SI). Supplementary information is available. See DOI: https://doi.org/10.1039/d6ma00092d.

Additional experimental data, characterization results, and electrochemical measurements generated during the current study are available from the corresponding authors upon reasonable request.

Acknowledgements

The authors gratefully acknowledge Mr Mohammed A. Alkhamisah and Mr Abdulrahman A. Alghihab for their technical support and assistance. This work was supported by a research grant from the Research, Development, and Innovation Authority (RDIA), Kingdom of Saudi Arabia (grant no. 12866-KACST-2023-KACST-R-2-1-EI).

References

1 S. Chu, Y. Cui and N. Liu, The path towards sustainable energy, *Nat. Mater.*, 2017, **16**, 16–22.
2 J. Hickel and G. Kallis, Is Green Growth Possible?, *New Political Econ.*, 2020, **25**, 469–486.
3 T. Capurso, M. Stefanizzi, M. Torresi and S. M. Camporeale, Perspective of the role of hydrogen in the 21st century energy transition, *Energy Convers. Manage.*, 2022, **251**, 114898.
4 A. Fujishima and K. Honda, Electrochemical Photolysis of Water at a Semiconductor Electrode, *Nature*, 1972, **238**, 37–38.
5 M. Grätzel, Photoelectrochemical cells, *Nature*, 2001, **414**, 338–344.
6 M. G. Walter, *et al.*, Solar Water Splitting Cells, *Chem. Rev.*, 2010, **110**, 6446–6473.
7 N. S. Lewis and D. G. Nocera, Powering the planet: Chemical challenges in solar energy utilization, *Proc. Natl. Acad. Sci. U. S. A.*, 2006, **103**, 15729–15735.
8 A. Kudo and Y. Miseki, Heterogeneous photocatalyst materials for water splitting, *Chem. Soc. Rev.*, 2009, **38**, 253–278.
9 F. E. Osterloh, Inorganic Materials as Catalysts for Photochemical Splitting of Water, *Chem. Mater.*, 2008, **20**, 35–54.
10 K. Sivula and R. Van De Krol, Semiconducting materials for photoelectrochemical energy conversion, *Nat. Rev. Mater.*, 2016, **1**, 15010.
11 X. Yu, T. J. Marks and A. Facchetti, Metal oxides for optoelectronic applications, *Nat. Mater.*, 2016, **15**, 383–396.
12 J. Seo, H. Nishiyama, T. Yamada and K. Domen, Visible-Light-Responsive Photoanodes for Highly Active, Stable Water Oxidation, *Angew. Chem. Int. Ed.*, 2018, **57**, 8396–8415.
13 S. Corby, *et al.*, Charge Separation, Band-Bending, and Recombination in WO $_3$ Photoanodes, *J. Phys. Chem. Lett.*, 2019, **10**, 5395–5401.
14 M. Xiao, B. Luo, Z. Wang, S. Wang and L. Wang, Recent Advances of Metal-Oxide Photoanodes: Engineering of Charge Separation and Transportation toward Efficient Solar Water Splitting, *Sol. RRL*, 2020, **4**, 1900509.
15 N. Guijarro, M. S. Prévot and K. Sivula, Surface modification of semiconductor photoelectrodes, *Phys. Chem. Chem. Phys.*, 2015, **17**, 15655–15674.
16 R. Chen, L. Meng, W. Xu and L. Li, Cocatalysts-Photoanode Interface in Photoelectrochemical Water Splitting: Understanding and Insights, *Small*, 2024, **20**, 2304807.
17 B. S. Kalanoor, H. Seo and S. S. Kalanur, Recent developments in photoelectrochemical water-splitting using WO_3/$BiVO_4$ heterojunction photoanode: A review, *Mater. Sci. Energy Technol.*, 2018, **1**, 49–62.
18 X. Cheng, Y. Zhang, H. Hu, M. Shang and Y. Bi, High-efficiency $SrTiO_3$/TiO_2 hetero-photoanode for visible-light water splitting by charge transport design and optical absorption management, *Nanoscale*, 2018, **10**, 3644–3649.
19 S. Li, W. Xu, L. Meng, W. Tian and L. Li, Recent Progress on Semiconductor Heterojunction-Based Photoanodes for Photoelectrochemical Water Splitting, *Small Sci.*, 2022, **2**, 2100112.
20 S. Bai, *et al.*, Bi nanoparticles modified the WO_3/$ZnWO_4$ heterojunction for photoelectrochemical water splitting, *J. Colloid Interface Sci.*, 2023, **646**, 745–752.
21 A. M. Alotaibi, *et al.*, Surface engineering of CuO-Cu_2O heterojunction thin films for improved photoelectrochemical water splitting, *Renewable Energy*, 2024, **235**, 121326.
22 K. Syrek, *et al.*, Surface Engineering of Anodic WO $_3$ Layers by In Situ Doping for Light-Assisted Water Splitting, *ACS Appl. Mater. Interfaces*, 2024, **16**(28), 36752–36762.
23 Z. Masoumi, M. Tayebi and B.-K. Lee, The role of doping molybdenum (Mo) and back-front side illumination in enhancing the charge separation of α-Fe_2O_3 nanorod photoanode for solar water splitting, *Sol. Energy*, 2020, **205**, 126–134.
24 A. M. Huerta-Flores, G. Chávez-Angulo, O. A. Carrasco-Jaim, L. M. Torres-Martínez and M. A. Garza-Navarro, Enhanced photoelectrochemical water splitting on heterostructured α-Fe_2O_3–TiO_2:X (X = Co, Cu, Bi) photoanodes: Role of metal doping on charge carrier dynamics improvement, *J. Photochem. Photobiol., A*, 2021, **410**, 113077.
25 F. Wang, C. Di Valentin and G. Pacchioni, Doping of WO $_3$ for Photocatalytic Water Splitting: Hints from Density Functional Theory, *J. Phys. Chem. C*, 2012, **116**, 8901–8909.
26 Y. Liu, *et al.*, Electrochemical Doping Induced *In Situ* Homo-species for Enhanced Photoelectrochemical Performance on WO_3 Nanoparticles Film Photoelectrodes, *Electrochim. Acta*, 2016, **210**, 251–260.
27 S. S. Kalanur, R. Singh and H. Seo, Enhanced solar water splitting of an ideally doped and work function tuned {002} oriented one-dimensional WO_3 with nanoscale surface charge mapping insights, *Appl. Catal., B*, 2021, **295**, 120269.
28 G. Hodes, D. Cahen and J. Manassen, Tungsten trioxide as a photoanode for a photoelectrochemical cell (PEC), *Nature*, 1976, **260**, 312–313.

© 2026 The Author(s). Published by the Royal Society of Chemistry

Open Access Article. Published on 29 June 2026. Downloaded on 6/30/2026 1:33:55 AM.
This article is licensed under a Creative Commons Attribution 3.0 Unported Licence.

29 S. Speldrich, M. Wark and G. Wittstock, Metal Oxide Protection Layers for Enhanced Stability and Activity of WO $_3$ Photoanodes in Alkaline Media, *ACS Appl. Energy Mater.*, 2023, **6**, 9602–9614.

30 W. L. Kwong, C. C. Lee and J. Messinger, Transparent Nanoparticulate FeOOH Improves the Performance of a WO $_3$ Photoanode in a Tandem Water-Splitting Device, *J. Phys. Chem. C*, 2016, **120**, 10941–10950.

31 P. Chatterjee and A. K. Chakraborty, Enhanced photoelectrochemical water oxidation by Fe(II) modified nanostructured WO_3 photoanode, *Opt. Mater.*, 2023, **144**, 114361.

32 M. Yang, *et al.*, Enhanced photoelectrochemical water oxidation on WO_3 nanoflake films by coupling with amorphous TiO_2, *Electrochim. Acta*, 2018, **283**, 871–881.

33 M. A. Butler, R. D. Nasby and R. K. Quinn, Tungsten trioxide as an electrode for photoelectrolysis of water, *Solid State Commun.*, 1976, **19**, 1011–1014.

34 S. S. Kalanur, I.-H. Yoo and H. Seo, Fundamental investigation of Ti doped WO_3 photoanode and their influence on photoelectrochemical water splitting activity, *Electrochim. Acta*, 2017, **254**, 348–357.

35 S. S. Kalanur, I.-H. Yoo, K. Eom and H. Seo, Enhancement of photoelectrochemical water splitting response of WO_3 by Means of Bi doping, *J. Catal.*, 2018, **357**, 127–137.

36 X. Li, M. Ai, X. Zhang, J.-J. Zou and L. Pan, Dual co-catalysts decorated Zn-WO_3 nanorod arrays with highly efficient photoelectrocatalytic performance, *Int. J. Hydrogen Energy*, 2022, **47**, 13641–13653.

37 A. Hameed, M. A. Gondal and Z. H. Yamani, Effect of transition metal doping on photocatalytic activity of WO_3 for water splitting under laser illumination: role of 3d-orbitals, *Catal. Commun.*, 2004, **5**, 715–719.

38 H. Song, *et al.*, Synthesis of Fe-doped WO_3 nanostructures with high visible-light-driven photocatalytic activities, *Appl. Catal., B*, 2015, **166–167**, 112–120.

39 T. Zhang, *et al.*, Iron-doping-enhanced photoelectrochemical water splitting performance of nanostructured WO $_3$: a combined experimental and theoretical study, *Nanoscale*, 2015, **7**, 2933–2940.

40 R. B. Ali, Y. J. Lee, Q. A. Sial, L. T. Duy and H. Seo, A new insight into vacancy modulation in lead-doped tungsten oxide nanoarchitect for photoelectrochemical water splitting: An experimental and density functional theory approach, *J. Colloid Interface Sci.*, 2024, **665**, 19–31.

41 D. Madhan, M. Parthibavarman, P. Rajkumar and M. Sangeetha, Influence of Zn doping on structural, optical and photocatalytic activity of WO_3 nanoparticles by a novel microwave irradiation technique, *J. Mater. Sci.: Mater. Electron.*, 2015, **26**, 6823–6830.

42 K. Sivula, F. Le Formal and M. Grätzel, Solar Water Splitting: Progress Using Hematite (α-Fe_2O_3) Photoelectrodes, *ChemSusChem*, 2011, **4**, 432–449.

43 A. Samanta, M. N. Goswami and P. K. Mahapatra, Influence of Nd^{3+} doping in ZnO nanoparticles to enhance the optical and photocatalytic activity, *Mater. Res. Express*, 2019, **6**, 065031.

44 Z. Jiao, X. W. Sun, J. Wang, L. Ke and H. V. Demir, Hydrothermally grown nanostructured WO_3 films and their electrochromic characteristics, *J. Phys. D: Appl. Phys.*, 2010, **43**, 285501.

45 Y. Djaoued, S. Priya and S. Balaji, Low temperature synthesis of nanocrystalline WO_3 films by sol–gel process, *J. Non-Cryst. Solids*, 2008, **354**, 673–679.

46 S. Singh, P. Gurawal, G. Malik, D. Kaur and R. Chandra, Temperature-dependent wetting and other physical characteristics of sputtered grown WO_3 thin films, *Bull. Mater. Sci.*, 2024, **47**, 137.

47 P.-K. Lin, Y. Qin, X. Qi and L. Huang, Improved isoprene detection performance of Si-doped WO_3 films deposited by sputtering and post-annealing, *RSC Adv.*, 2024, **14**, 13618–13627.

48 F. Wan, *et al.*, Plasma assisted pulsed laser deposition of WO_3 films for thermochromism, *Mater. Chem. Phys.*, 2024, **314**, 128880.

49 A. Sh Maktoof, G. H. Mohammed and H. H. Abbas, Effect of annealing process on structural and optical properties of Au-doped thin films (NiO:WO_3) fabricated by PLD technique, *J. Opt.*, 2024, **54**, 2204–2215.

50 S. N. Ariffin, H. N. Lim, Z. A. Talib, A. Pandikumar and N. M. Huang, Aerosol-assisted chemical vapor deposition of metal oxide thin films for photoelectrochemical water splitting, *Int. J. Hydrogen Energy*, 2015, **40**, 2115–2131.

51 X. Hou and K.-L. Choy, Processing and Applications of Aerosol-Assisted Chemical Vapor Deposition, *Chem. Vap. Deposition*, 2006, **12**, 583–596.

52 M. Ling and C. Blackman, Growth mechanism of planar or nanorod structured tungsten oxide thin films deposited via aerosol assisted chemical vapour deposition (AACVD), *Phys. Status Solidi C*, 2015, **12**, 869–877.

53 S. Vallejos, P. Umek and C. Blackman, Aerosol Assisted Chemical Vapour Deposition Control Parameters for Selective Deposition of Tungsten Oxide Nanostructures, *J. Nanosci. Nanotechnol.*, 2011, **11**, 8214–8220.

54 H. H. Afify, S. A. Hassan, M. Obaida, I. Moussa and A. Abouelsayed, Preparation, characterization, and optical spectroscopic studies of nanocrystalline tungsten oxide WO_3, *Opt. Laser Technol.*, 2019, **111**, 604–611.

55 Q. Jia, H. Ji and X. Bai, Selective sensing property of triclinic WO_3 nanosheets towards ultra-low concentration of acetone, *J. Mater. Sci.: Mater. Electron.*, 2019, **30**, 7824–7833.

56 X. Li, Y. Wang, W. Liu, G. Jiang and C. Zhu, Study of oxygen vacancies′ influence on the lattice parameter in ZnO thin film, *Mater. Lett.*, 2012, **85**, 25–28.

57 A. Paliwal, A. Sharma, M. Tomar and V. Gupta, Optical properties of WO_3 thin films using surface plasmon resonance technique, *J. Appl. Phys.*, 2014, **115**, 043104.

58 Y. Zhu and C. S. Blackman, Aerosol-Assisted Chemical Vapour Deposition (AACVD) of Silver Nanoparticle Decorated Tungsten Oxide Nanoneedle for Use in Oxygen Gas Sensing.

59 M. Ling, Tungsten Oxide and Tungsten Oxide Based Heterogeneous Nanostructure thin films: Synthesis *via* AACVD, Characterisation, Growth Mechanism, and Application in Photocatalysis.

© 2026 The Author(s). Published by the Royal Society of Chemistry

Open Access Article. Published on 29 June 2026. Downloaded on 6/30/2026 1:33:55 AM.
This article is licensed under a Creative Commons Attribution 3.0 Unported Licence.

60 S. Phanichphant, A. Nakaruk, K. Chansaenpak and D. Channei, Evaluating the photocatalytic efficiency of the $BiVO_4$/rGO photocatalyst, *Sci. Rep.*, 2019, **9**, 16091.

61 S. Park, H. Kim, C. Jin and C. Lee, Intense ultraviolet emission from needle-like WO_3 nanostructures synthesized by noncatalytic thermal evaporation, *Nanoscale Res. Lett.*, 2011, **6**, 451.

62 E. M. Ngigi, P. N. Nomngongo and J. C. Ngila, Synthesis and Application of Fe-Doped WO_3 Nanoparticles for Photocatalytic Degradation of Methylparaben Using Visible–Light Radiation and H_2O_2, *Catal. Lett.*, 2019, **149**, 49–60.

63 Y. Shabdan, A. Markhabayeva, N. Bakranov and N. Nuraje, Photoactive Tungsten-Oxide Nanomaterials for Water-Splitting, *Nanomaterials*, 2020, **10**, 1871.

64 F. Zhan, *et al.*, Boric acid assisted synthesis of WO_3 nanostructures with highly reactive (002) facet and enhanced photoelectrocatalytic activity, *J. Mater. Sci.: Mater. Electron.*, 2017, **28**, 13836–13845.

65 D. Chandra, *et al.*, Temperature-Controlled Transformation of WO_3 Nanowires into Active Facets-Exposed Hexagonal Prisms toward Efficient Visible-Light-Driven Water Oxidation, *ACS Appl. Mater. Interfaces*, 2023, **15**, 20885–20896.

66 S. S. Kalanur, I.-H. Yoo and H. Seo, Fundamental investigation of Ti doped WO_3 photoanode and their influence on photoelectrochemical water splitting activity, *Electrochim. Acta*, 2017, **254**, 348–357.

67 M. Kumar Mohanta, T. Kanta Sahu, S. Alam and M. Qureshi, Tuning the Electronic Structure of Monoclinic Tungsten Oxide Nanoblocks by Indium Doping for Boosted Photoelectrochemical Performance, *Chem. – Asian J.*, 2020, **15**, 3886–3896.

68 S. Jafarpour and H. Naghshara, Reactive co-sputter deposition of Ta-doped tungsten oxide thin films for water splitting application, *Sci. Rep.*, 2025, **15**, 8302.

69 S. S. Kalanur, Structural, Optical, Band Edge and Enhanced Photoelectrochemical Water Splitting Properties of Tin-Doped WO_3, *Catalysts*, 2019, **9**, 456.

70 W. Li, *et al.*, Enhancing photoelectrochemical water splitting by aluminum-doped plate-like WO_3 electrodes, *Electrochim. Acta*, 2015, **160**, 57–63.

71 Y.-H. Xiao, C.-Q. Xu and W.-D. Zhang, Facile synthesis of Ni-doped WO_3 nanoplate arrays for effective photoelectrochemical water splitting, *J. Solid State Electrochem.*, 2017, **21**, 3355–3364.

72 S. S. Kalanur, Y.-G. Noh and H. Seo, Engineering band edge properties of WO_3 with respect to photoelectrochemical water splitting potentials via a generalized doping protocol of first-row transition metal ions, *Appl. Surf. Sci.*, 2020, **509**, 145253.

73 Y. Liu, *et al.*, Enhancement of the Photoelectrochemical Performance of WO_3 Vertical Arrays Film for Solar Water Splitting by Gadolinium Doping, *J. Phys. Chem. C*, 2015, **119**, 14834–14842.

74 O. Savadogo, Correlation between the flat band potential of semiconductors and solvent donor numbers, *Mater. Res. Bull.*, 1988, **23**, 1451–1458.

75 C. Jiang, S. J. A. Moniz, A. Wang, T. Zhang and J. Tang, Photoelectrochemical devices for solar water splitting – materials and challenges, *Chem. Soc. Rev.*, 2017, **46**, 4645–4660.

76 A. R. Chard and J. B. Sambur, Measuring the flatband potential in 2D semiconductors: Pitfalls and a possible SECCM solution, *Curr. Opin. Electrochem.*, 2025, **52**, 101703.

77 E. Koshevoy, *et al.*, Photoelectrochemical Methods for the Determination of the Flat-Band Potential in Semiconducting Photocatalysts: A Comparison Study, *Langmuir*, 2023, **39**, 13466–13480.

78 A. Hankin, F. E. Bedoya-Lora, J. C. Alexander, A. Regoutz and G. H. Kelsall, Flat band potential determination: avoiding the pitfalls, *J. Mater. Chem. A*, 2019, **7**, 26162–26176.

79 S. Al-Hilli and M. Willander, The pH Response and Sensing Mechanism of n-Type ZnO/Electrolyte Interfaces, *Sensors*, 2009, **9**, 7445–7480.

© 2026 The Author(s). Published by the Royal Society of Chemistry